J Solid State Electrochem (2008) 12:729–737
DOI 10.1007/s10008-007-0420-3

ORIGINAL PAPER

Electrochemical evaluation of $CuFe_2O_4$ samples obtained by sol–gel methods used as anodes in lithium batteries

M. Bomio · P. Lavela · J. L. Tirado

Received: 8 May 2007 / Accepted: 23 August 2007 / Published online: 21 September 2007

Abstract $CuFe_2O_4$ with a tetragonally distorted spinel structure has been prepared by the thermal decomposition of a citrate precursor. The copper–iron mixed organic salt was precipitated by either water evaporation or ethanol dehydration. The level of impurities of the final products depended on the precursor precipitation route and annealing temperature. EDH(800) material performed capacity values of 520 mAh/g after 50 cycles. Electron microscopy evidenced that the extrusion of copper yielded both transition metals separately at the end of discharge.

Keywords Lithium · Batteries · Sol–gel · Citrate · Ferrite

Introduction

Decades ago, a survey of the reactivity of numerous binary compounds M_xO_y towards Li at low voltage was carried out. The research efforts were focused on active solids in electrochemical insertion reactions. The well-established reversibility of the intercalation mechanism assured the rechargeability of the battery built with insertion electrode materials. These electrochemical reactions were commonly tested at voltages higher than 1.0 V. Above this cut off voltage, the electron consumption usually justifies both the partial reduction of the metallic atoms and the occupancy of empty sites in the structure. For lower cell potentials, some electrochemical and structural data obtained by Thackeray's group on iron oxides were regarded as the consequence of an insertion of lithium into, and iron extrusion from, the cubic close-packed lattice. The products of a complete discharge were identified as Li_2O and α-Fe [1].

The potential use of binary transition metal oxides (M_xO_y with M = Fe, Cu, Co, and Ni) as anode materials for lithium ion batteries was recently reinforced [2]. Tarascon's group proposed a mechanism of the lithium reaction that differs from either the conventional lithium insertion/extraction in graphite or the formation of lithium–tin intermetallics. These authors proposed the reversible reduction of the transition metal to the metallic state along the formation of Li_2O—conversion reaction—according the following equation:

$$M_xO_y + 2ye^- + 2yLi^+ \underset{\text{Charge}}{\overset{\text{Discharge}}{\rightleftharpoons}} xM^0 + yLi_2O \qquad (1)$$

The extended reduction of the metal atoms leads to cell capacity values as high as 700 mAh/g for CoO [3]. If the $\Delta G_f^o(Li_2O) = -561.2\ kJmol^{-1}$ is compared with $\Delta G_f^o(CoO) = -214.2 kJmol^{-1}$ the exoergicity of reaction (1) is clearly predictable.

Assuming that the only condition for the feasibility of this redox reaction is exoergicity, other transition metal compounds such as nickel and iron oxides are possible electrode candidates. In fact, these oxides have been also researched to evaluate the electrochemical performance in lithium cells [3]. In addition, other compounds including chalcogenides [4, 5], halides [6], phosphides [7], oxysalts [8] are demonstrated to undergo conversion reactions. However, some drawbacks as the Li_2S solubility or low electronic conductivity of fluorides hinder an electrochemical behavior as performing as that of the oxides.

M. Bomio · P. Lavela (✉) · J. L. Tirado
Laboratorio de Química Inorgánica, Universidad de Córdoba,
Campus de Rabanales,
14071 Córdoba, Spain
e-mail: iq1lacap@uco.es

A different research topic is the evaluation of mixed transition metal oxides. The reversibility of conversion reactions in compounds such as $NiCo_2O_4$ [9, 10] and $NiFe_2O_4$ [11] has been evidenced. Moreover, Kalaiselvi et al. have studied $CuFe_2O_4/SnO_2$ composites as a mean to improve the electrochemical behavior of this copper ferrite [12].

It is accepted that conversion reactions are affected by composition, particle size and morphology, which in turn are directly related to the preparation procedure [13]. Soft-chemistry techniques are suitable for the synthesis of ultrafine materials with homogeneous composition and adequate morphology for their use in multiple technological purposes. Sol–gel and organic precursor methods have been extensively used for the preparation of cathode materials [14]. By using citrate precursors, the chelating agent ensures the homogeneous distribution of transition metals at an atomic scale in the citrate precursors. In the case of mixed oxides, this fact favors the formation of a pure phase instead of a mixture of binary oxides.

The aim of this work is the synthesis and electrochemical characterization of $CuFe_2O_4$ preparations from different sol–gel methods based on a citrate precursor to determine the influence of particle morphology in the efficiency of the conversion reaction allowing the reversible lithium reaction and consequently their performance as anode material for lithium cells.

Materials and methods

$CuFe_2O_4$ samples were synthesized by a two-step procedure including the preparation of a metal citrate precursor and its thermal decomposition to obtain the transition metal oxide. A solution was prepared by dissolving $Fe(NO_3)_3{\cdot}9H_2O$ (Panreac 98.0) and $Cu(NO_3)_2{\cdot}3H_2O$ (Panreac 99.0) in 80 ml of water to achieve a 0.3 M metal concentration and the 2:1 stoichiometric ratio. Then, a stoichiometric amount of citric acid (Panreac 99.5) was added to reach the 1:1 metal:ligand ratio (a slightly excess less than 10% of the acid was allowed to assure the complete chelation of the metal ions). Eventually, the solution was neutralized by adding ammonium hydroxide 30%.

The solid precursor was then precipitated by two alternative procedures: (1) Solvent evaporation at 80 °C to obtain a sol, which was further dried at 120 °C. The samples prepared from this precursor will be named as water heating evaporation (WHE), (2) an ethanol dehydration process was alternatively performed by slowly pouring 400 ml of absolute ethanol on the aqueous solution. The mixed aqueous-ethylic solution was stirred at room temperature until a gel was precipitated and then dried. These samples will be named as ethanol dehydration (EDH). The citrate precursors were further annealed at different temperatures ranging from 600 to 1,000 °C for 6 h in air. The heating and cooling ramps were set to 5 °C/min. For clarity purposes, $CuFe_2O_4$ samples will be named herein by the precursor acronym followed by the annealing temperature between brackets, e.g., WHE(800).

The X-Ray diffraction patterns were obtained using a Siemens *D5000 Diffractometer*, with a CuKα radiation (1.5406 Å) and graphite as monochromator. Scaning microscopy was performed on a *JEOL-SM6300* microscope provided with Energy Dispersive X-ray Spectrometry (EDS).

The thermal decomposition of the precursor was evaluated in a Setaram Setsys 12, under a synthetic air atmosphere with a gas flux of 70 ml/min. The heating rate was set at 10 °C/min, and the final temperature was 1,000 °C. A reference material, α-Al_2O_3, was needed in DTA measurement. Fourier Transform Infrared spectra were recorded in an FT-MIR *Nicolet Magna-IR550 Series II spectrometer*. Resolution was set at 4 cm^{-1} in the spectral range covering 4,000–400 cm^{-1}. The sample pellets were prepared using 100 mg of dry KBr and 1 mg of the metal citrate products.

The surface area measurements were carried out in a *Micromeritics ASAP 2000*. The samples were previously degassed at 150 °C under 0.04 μmHg pressure during 12 h to remove traces of water and adsorbed gases.

Electrochemical tests were performed in two and three electrodes Swagelok-type cells were assembled inside a MBraun LabMaster 130 glove box under argon atmosphere with less than 2 ppm of H_2O and O_2. Lithium metal disk, 9 mm diameter, was used as auxiliary and reference. The electrolyte solution (1 M $LiPF_6$ in 1:1 *w*/*w* EC:DEC) was supported by two porous glass-paper (GF/A-Whatman) disks also acting as separator.

Electrodes containing the studied samples were fabricated from a mixture containing 75% of active material, 10% carbon black, 10% graphite, and 5% of polyvinylidene fluoride (PVDF). A paste is prepared by soaking this mixture in *N*-methyl-2-pyrrolidone (NMP) which is eventually spread onto a 9-mm diameter copper foil (Goodfellow 99.999%). The electrode was dried at 120 °C and 7 mbar for 4 h and pressed under a 1 ton load to ensure a uniform surface.

Galvanostatic battery testing was carried out in two electrodes Li/1 M $LiPF_6$(EC:DEC)/$CuFe_2O_4$. Current control and cell potential measurements during charge and discharge were carried out with a multichannel galvanostat *Arbin Instruments*. This equipment controls current conditions during charging and discharging and monitors the cell potential and test time. Electrochemical Impedance Spectra (EIS) were recorded from three electrode Swagelok-type

cells. The test cell was previously discharged to a definite depth of discharge and allowed to relax for at least 5 h. The AC measurements were made in *AUTOLAB PGSTAT 12* with a 5-mV amplitude and frequency range between 100 kHz and 2 mHz.

Results and discussion

The X-ray diffraction (XRD) patterns of the as-prepared metal–citrates are characterized by a set of reflections ascribable to NH_4NO_3, precipitated upon solvent removal from the NH_4^+ and NO_3^- ions coming from the pH adjusting procedure and the metal salt reactants, respectively. Yue et al. have demonstrated that crystalline NH_4NO_3 commonly appears for pH values higher than 4 [15]. No reflections ascribable to metal citrates were observed, whichever the precursor measured.

The organic part of the metal citrate precursors was characterized by Fourier Transform Infrared (FTIR) (Fig. 1). The FTIR spectrum of citric acid is also shown for comparison, particularly to check the deprotonation of citric acidic to yield the citrate ligand in the precursor, and thus, giving an indirect evidence of the metal complexation process. In the spectral range of stretching vibrations of OH, the narrow bands at 3,496 and 3,450 cm^{-1} and the broad bands at 3,291 and 3,218 cm^{-1} clearly show that a complex network of hydrogen bonding exists in the citric acid (Fig. 1a). For all the citrate salts, a broad band at 3,140 cm^{-1} can be observed and assigned to the stretching of protonated hydroxyl groups. In addition, a diffuse band at 3,500 cm^{-1} is usually assigned to crystallization and/or coordination water. One of the most characteristic vibrations in infrared measurements for citric acid is the presence of an OH group in a tertiary carbon. Its presence is evidenced by the bands located at 1,380–1,350 cm^{-1} and 1,190-1,100 cm^{-1}. These bands are associated to the bending and stretching vibrations of OH and C–O(H), respectively (Fig. 1b).

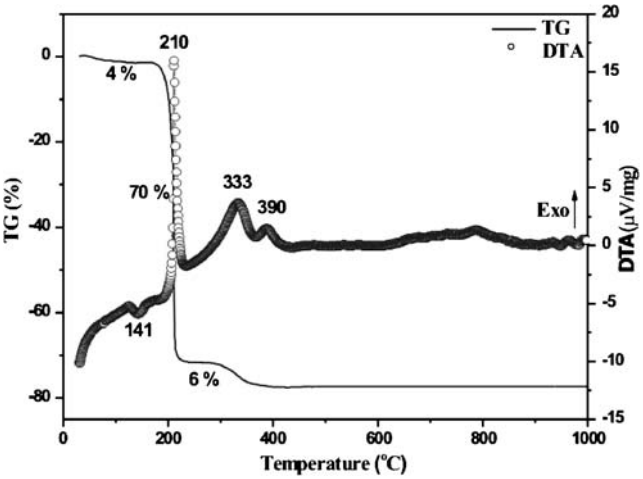

Fig. 2 DTA and TG plot of the WHE dried precursor

The deprotonation of citric acid into citrate anions can be followed by the changes of five characteristic vibrations of –COOH, corresponding to $\nu_{C=O}$=1,754 and 1,702 cm^{-1}; $\delta_{OH(in\text{-}plane)}$=1,427 cm^{-1} ; $\nu_{C\text{-}O}$=1,300–1,130 cm^{-1} and $\delta_{OH\ (out\text{-}of\text{-}plane)}$=937.25 cm^{-1}, by two characteristic vibrations of $-CO_2^-$, corresponding to the antisymmetric and symmetric stretching vibrations centered near to 1,620 and 1,384 cm^{-1}, respectively [16].

Thermal analysis allows following the precursor decomposition during the heat treatment, which eventually will produce the oxide. Figure 2 shows the DTA and TG curves of the citrate precursors prepared by heating evaporation. A small endothermic effect was observed between 120 and 180 °C, which is due to the evaporation of residual solvent molecules absorbed by the solid precursor. Weight losses around 4% were determined for the release of absorbed water. A highly intense and narrow exothermic peak, at ca 210 °C, is responsible for a large weight loss, close to 70%. This signal is commonly assigned to the decomposition of

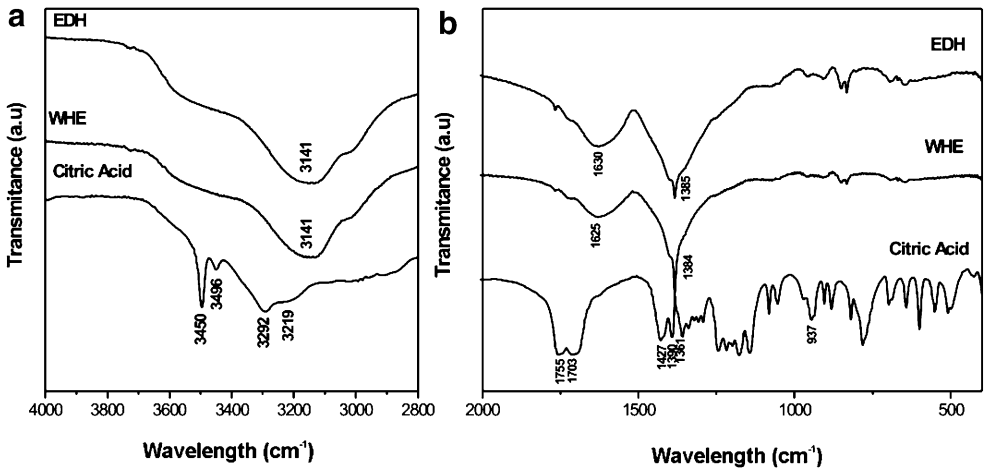

Fig. 1 a, **b** FTIR spectra of citric acid and precursor citrates

the organic molecules from metal citrate precursors with simultaneous evolution of CO and CO_2 gas [17]. These results disagree with the occurrence of dehydrated citrate precursors, as a 32% weight loss must be expected. Otherwise, the FTIR band located at ca 3,500 cm^{-1}, previously described, corresponding to coordination water actually means that a $CuFe_2(C_6H_5O_7)_3{\cdot}nH_2O$ stoichiometry must be present. Also, NH_4NO_3 may also decompose to NO_x and O_2 contributing to the overall loss [15]. A small exothermic effect was detected between 320 and 340 °C related to a weight loss of 6% is probably due to the release of residual organic material which was not completely burnt in the main decomposition process [18]. Finally, a small third exothermic peak located around 380–390 °C is usually assigned to the initial crystallization of the spinel copper ferrite [17]. From these results, it was decided to set

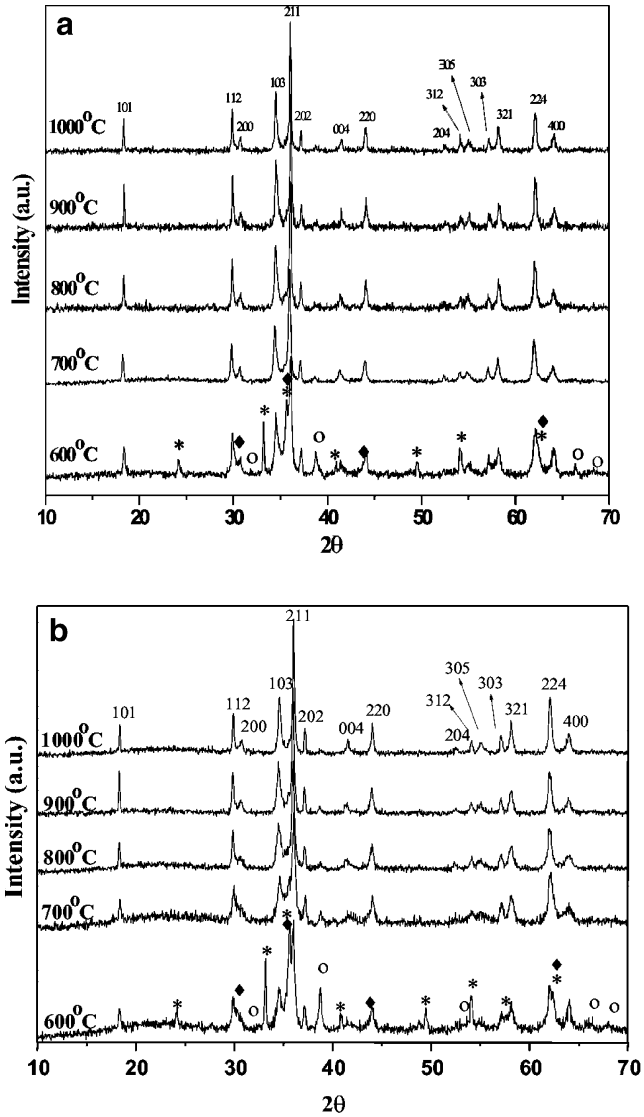

Fig. 3 XRD patterns of the copper ferrites annealed at several temperatures: **a** WHE, **b** EDH

Table 1 Average crystallite size for $CuFe_2O_4$ samples

Temperature (°C)	Average crystallite size (nm)	
	WHE	EDH
600	20.3	13.5
700	30.5	21.1
800	32	27.6
900	50.7	34.1
1,000	61.1	42.2

600 °C as the lowest annealing temperature to ensure the precursor decomposition.

$CuFe_2O_4$ has a tetragonal structure with a $I4_1/amd$ space group (34-425 JCPDS-ICDD card), regarded as a distorted cubic spinel structure. The d^9 electronic configuration state in Cu^{2+} ions favors the Jahn-Teller effect due to the elongation of the ligand axis along the d_z orbital. XRD of the annealed products obtained are shown in Fig. 3. At 600 °C, significant amounts of impurities were detected, including magnetite (◆ Fe_3O_4), hematite (* Fe_2O_3), and copper oxide (**o** CuO). The presence of impurities was negligible in WHE samples prepared above 700 °C, except for those obtained by ethanol dehydration. In EDH samples, a significant contribution of impurities was detected at 800 °C. Phase equilibria involving spinel solid solutions, delafossite, and hematite in the Fe–Cu–O system have been reported. Above 1,250 K, Fe_3O_4 and $CuFe_2O_4$ are known to form a continuous series of solid solutions [19].

Conversion reactions occur from the surface to the particle inner core. For this reason, particle size and morphology are expected to have a direct influence on the electrode performance. The average crystallite size, calculated from the line width of nonoverlapped reflections and using the Scherrer equation, is shown in Table 1. This value increased steadily up to 800 °C, and then, the size of the crystalline domains grew abruptly. For a same temperature, samples obtained by ethanol dehydration had always the lowest crystallite size. The sintering effect was also reflected in the BET surface values, whose values ranged from ca 10 m^2/g for samples annealed at 600 °C to less than 1 m^2/g when heated at 1,000 °C. Similar areas have been reported for related compounds [20].

SEM micrographs in Fig. 4 are evidences of significant differences in texture between samples obtained by the distinct procedures. At 600 °C, WHE sample is characterized by large aggregates surrounded by dispersed tiny particles, while massive particles are present for EDH oxide. By increasing the temperature to 800 °C, EDH(800) morphology changed to produce bulky secondary particles with big cavities extending into the particles, while WHE (800) suffered relatively small changes. At 1,000 °C, a

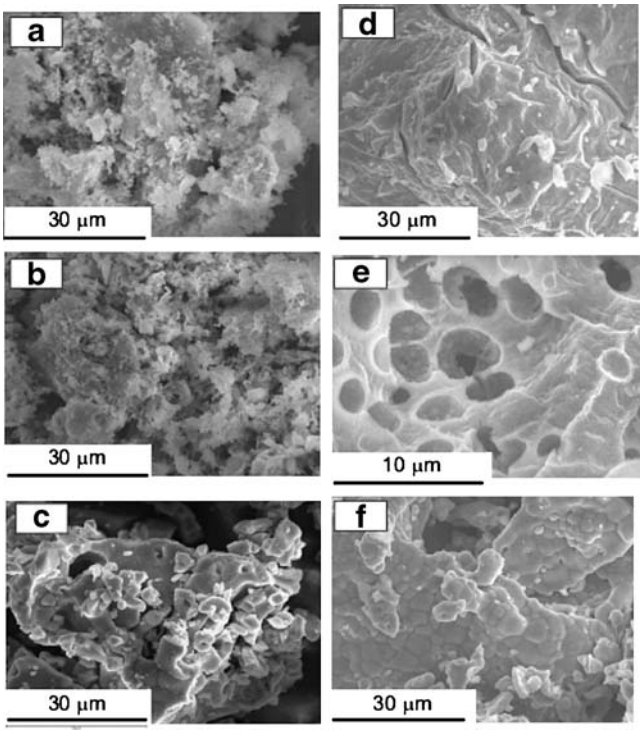

Fig. 4 SEM micrographs of $CuFe_2O_4$ samples. **a** WHE(600); **b** WHE (800); **c** WHE1000; **d** EDH(600); **e** EDH(800); **f** EDH(1000)

notorious growth of the primary particles was observed in both samples.

Because of the complete structural degradation upon metal reduction and the great influence of sample texture, EDH samples containing impurities were also evaluated. A point is yet to be discussed in this report, if particle morphology may positively influence the electrochemical performance, albeit minor amounts of impurities that were present in the sample.

The first discharge shows an initial plateau that extends to the charge needed for the complete transition metal reduction to the their metallic state. Then, a sloping voltage occurs until the lower cut off voltage is reached near 0 V (Fig. 5). A polymeric layer wrapping the reduced particles is expected at the end of the discharge [21]. The following charging curve is characterized by a high polarization and partial reversibility. The high surface energy of the reduced products greatly contributes to the potential in which the reverse conversion reaction takes place. However, the feasibility of the oxidation reaction is due to the presence of intimately mixed nanosized particles that are electrochemically produced in the discharge. Second and successive discharges revealed a different profile. The partial recovery of structure and morphology of the initial oxide generates energetically different sites for lithium reaction after the first charge [22, 23].

Quite similar profiles were recorded irrespective of the synthesis procedure. Copper and iron reduction in $CuFe_2O_4$ predominantly occurs through a ca 1.0-V plateau. This assessment is supported by the fact that this is the unique plateau in high temperature samples, where free impurities samples were detected by XRD. Moreover, this potential is an average value of those of the binary oxides. Capacity values reached values close to 1,000 mAh/g in the first discharge, although a significant loss of reversibility is detected after the first charge.

Additional plateaus at 1.37 and 1.25 V were detected for samples prepared at 600 °C (Fig. 5). They can be assigned to copper reduction from CuO and Cu_2O impurities, respectively [24]. These features appear along a new plateau at 0.9 V, which is coincident with that reported for hematite [25], which is what would confirm the incomplete formation of the mixed oxide at the lowest temperature. On increasing the annealing temperature, the CuO and Fe_2O_3

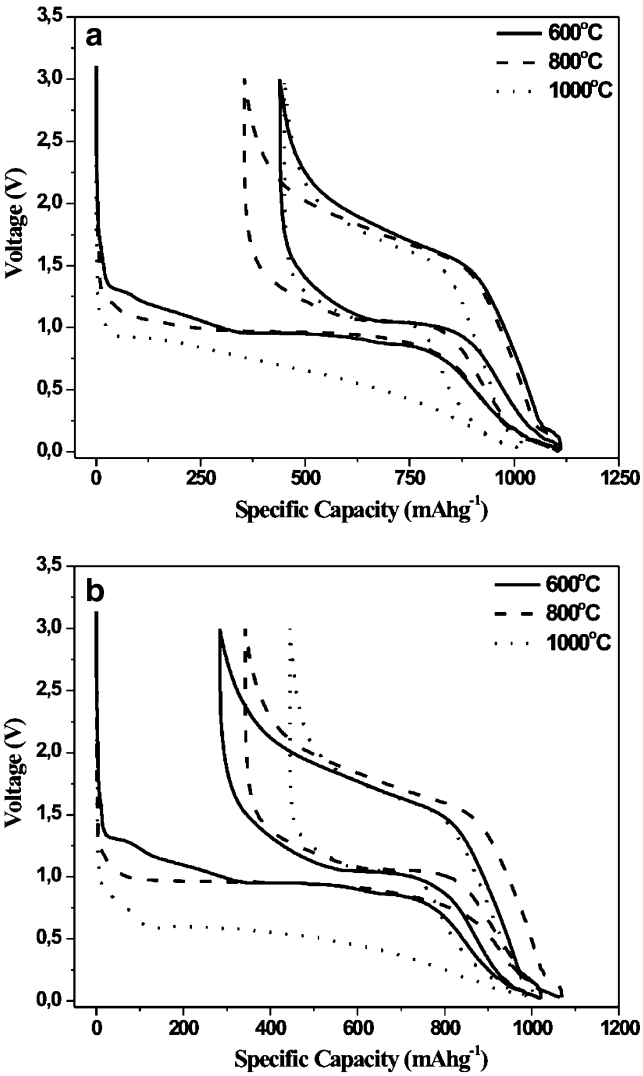

Fig. 5 Galvanostatic curves for the first and second discharge and first charge of lithium cells using $CuFe_2O_4$ samples prepared at several temperatures: **a** WHE, **b** EDH. Kinetic rate: 1C

reduction plateaus are further removed. The reversibility of these plateaus is not clear because they are absent in further cycles. Nevertheless, whether the metallic atoms reduced from the impurities are mixed with those of the pure phase cannot be discarded.

The first discharge curve of samples heated at 1,000 °C was considerably shorter and shifted to low voltages. Whether this behavior could be ascribed to kinetic effects or thermodynamic considerations deserved new experiments. Thus, the first discharge was recorded at rates ranging from C/5 to 5C (Fig. 6). Samples heated at 600 and 800 °C showed limited changes in cell potential and capacities in close range of variation, while for samples synthesized at 1,000 °C, more abrupt changes occurred. Therefore, the large particle size and low BET surface measured for this oxide undoubtedly make difficult the lithium reaction at a suitable rate.

The extended galvanostatic cycling is shown in Fig. 7. Samples obtained by the heating evaporation route were not able to sustain capacity upon cycling. At 600 °C, WHE(600) demonstrated a significant capacity fading, probably due to the uncompleted crystallization. The existence of a nonhomogeneous texture may greatly affect the cyclability of these materials. In contrast, values higher than 350 mAh/g were measured after 50 cycles for EDH(600), irrespective of the massive particles observed by SEM. Most likely, the crevasses on the surface provide a suitable path to lithium migration into these particles. EDH samples performed

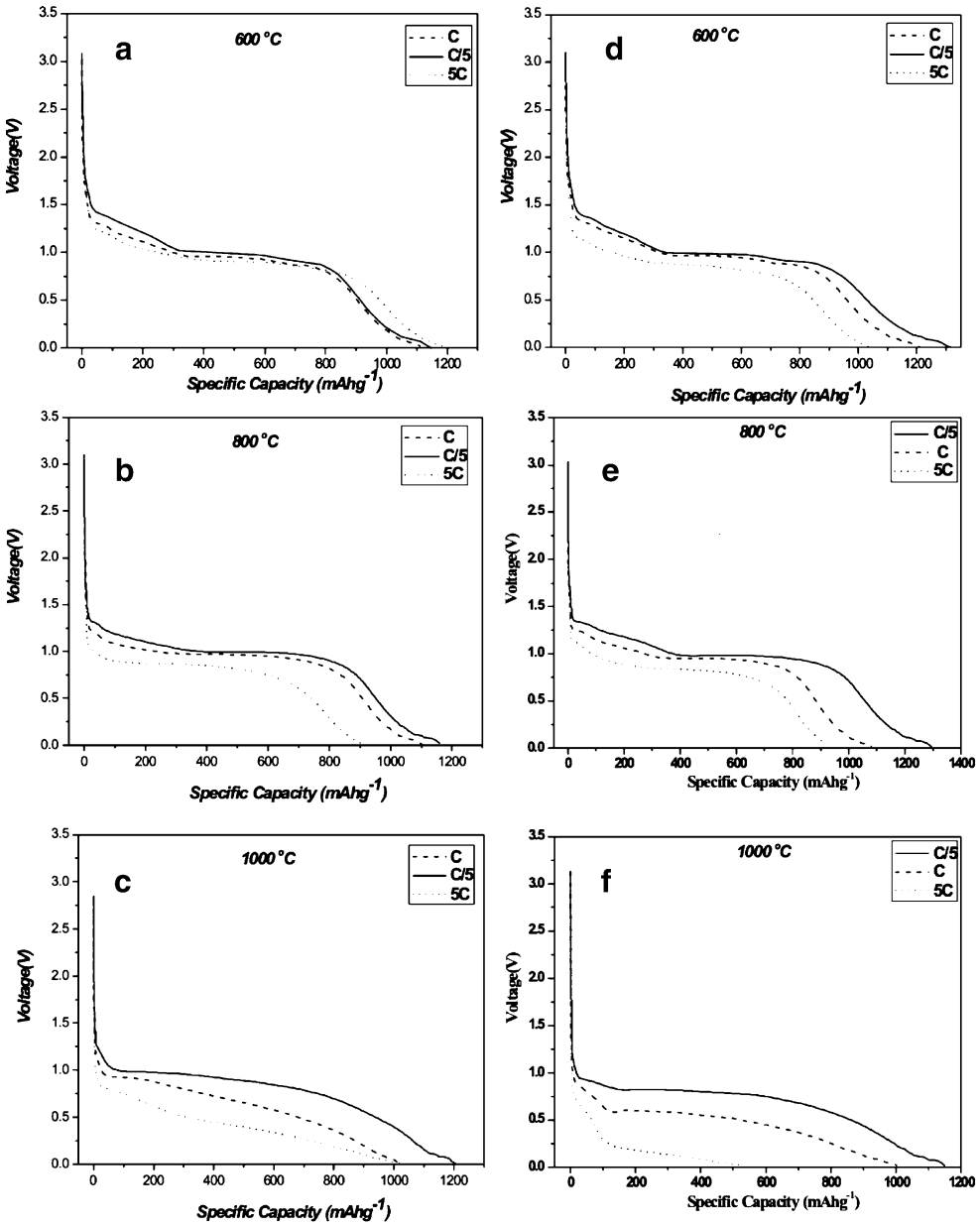

Fig. 6 First sweep of WHE (**a**–**c**) and EDH (**d**–**f**) samples discharged at different rates

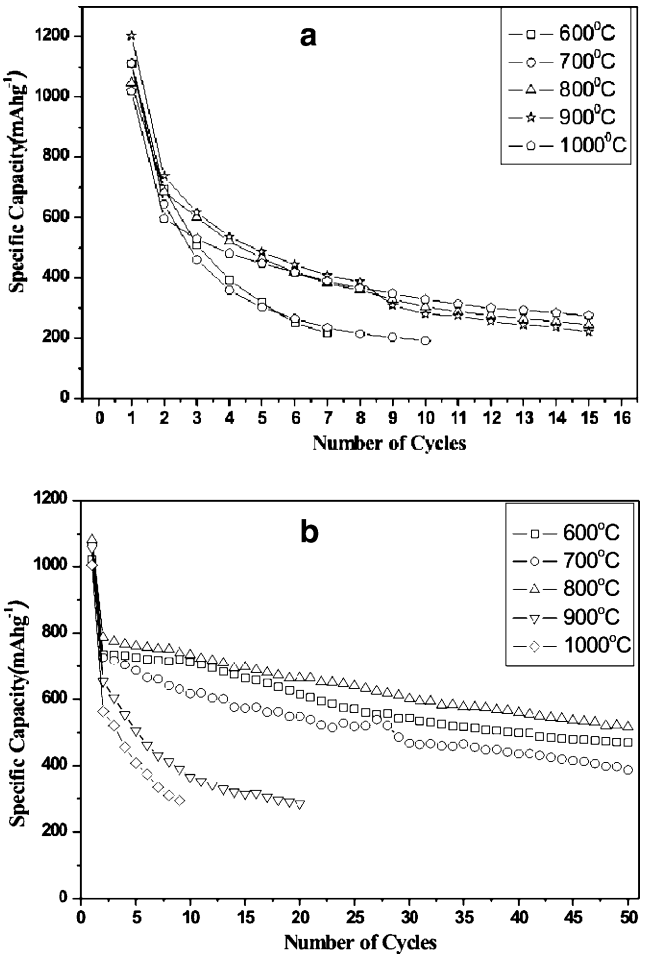

Fig. 7 Galvanostatic cycling of $CuFe_2O_4$ samples. **a** WHE and **b** EDH. Kinetic rate: 1C

better capacity retention than WHE oxides, except for samples prepared over 900 °C. These results are evidences that important amounts of binary oxides do not deteriorate the electrochemical performance of the samples. The main effect on the conversion reactions of these oxides is then related to particle morphology. The macroporous texture produced by the interconnection of nanoparticles in EDH (800) ensures a good electronic conductivity and contact between the oxide surface and the electrolyte solution. Values close to 500 mAh/g were retained after 50 cycles for this sample.

Electrochemical impedance spectroscopy has been used in this work to evaluate the kinetic response of samples produced at 800 °C by both chemical procedures. For this purpose, the spectra were recorded in different points of the first. Figure 8b shows a selected spectrum plotted as Nyquist plots. The profile is characterized by a semicircle at high frequencies and a nearly linear type frequency variation at low frequencies. Eventually, this last feature behaves as a very large semicircle when the scan is extended to very low frequencies. This last semicircle has been ascribed to a pseudo-capacitance-type behavior. The absence of a 45° straight line at low frequencies corresponding to a Warburg region was associated to the joint electronic conductivity and low ionic conductivity of the film that stands as a limited factor [21]. Our description will be focused on the two semicircles located at higher frequencies. Bearing in mind that these oxides have been described to grow an inorganic SEI on discharging, we can assign, by analogy with carbon-based electrodes [26], the first semicircle to the lithium migration through this film and the second one to the charge transfer process through the double layer on the electrode surface. The equivalent circuit used to fit the experimental data is shown in Fig. 8a. R_1 is the electrolyte solution resistance. The first depressed semicircle at a higher frequency interval (R_2Q_1) is ascribed to Li^+ migration through the solid electrolyte interface (SEI). The depression in the semicircle is currently associated to the presence of inhomogeneities in the electrode material such roughness, porosity, and/or polycrystalline state, which hinder the frequency dispersion in the interface [27]. The constant phase elements (Q) take into account the depression of the semicircles. A second depressed semicircle at a lower frequency (elements Q_2 and R_3 in parallel) is associated to charge transfer phenomena when lithium goes through the particle surface.

Figure 8c and d display the evolution of R_2 and R_3 values, respectively, through the first discharge. Initial R_2 values were higher for WHE(800) than for EDH(800). The different texture of these samples may influence greatly the nature of the SEI films. However, the drastic morphological changes occurring during the first discharge tend to match R_2 values at the end of the reduction plateau (ca 6 F/mol). From this point, SEI resistance values decreased for both samples.

R_3 values show a similar trend (Fig. 8d) for both samples. High values were recorded at the beginning of the discharge that decreases up to 3 F/mol. Then, the values were kept almost constant until the end of the discharge. Initial R_3 values for EDH(800) were significantly higher than those of WHE(800). Further discharge led to the opposite behavior. Considering the poor electronic conductivity of these oxides, the increase in metal content, provided by the conversion reaction, has a notorious influence on the kinetic response of these materials. Thus, we can deduce that the charge transfer reaction is enhanced when the discharge progresses. WHE (800) sample yielded the highest R_3 values in a wide range of discharge.

SEM micrograph was obtained for a WHE(1000) electrode discharged at 0 V (Fig. 9). The formation of the organic layer enveloping the particles is clearly evidenced. The degradation of the initial particles produces sharp-edge

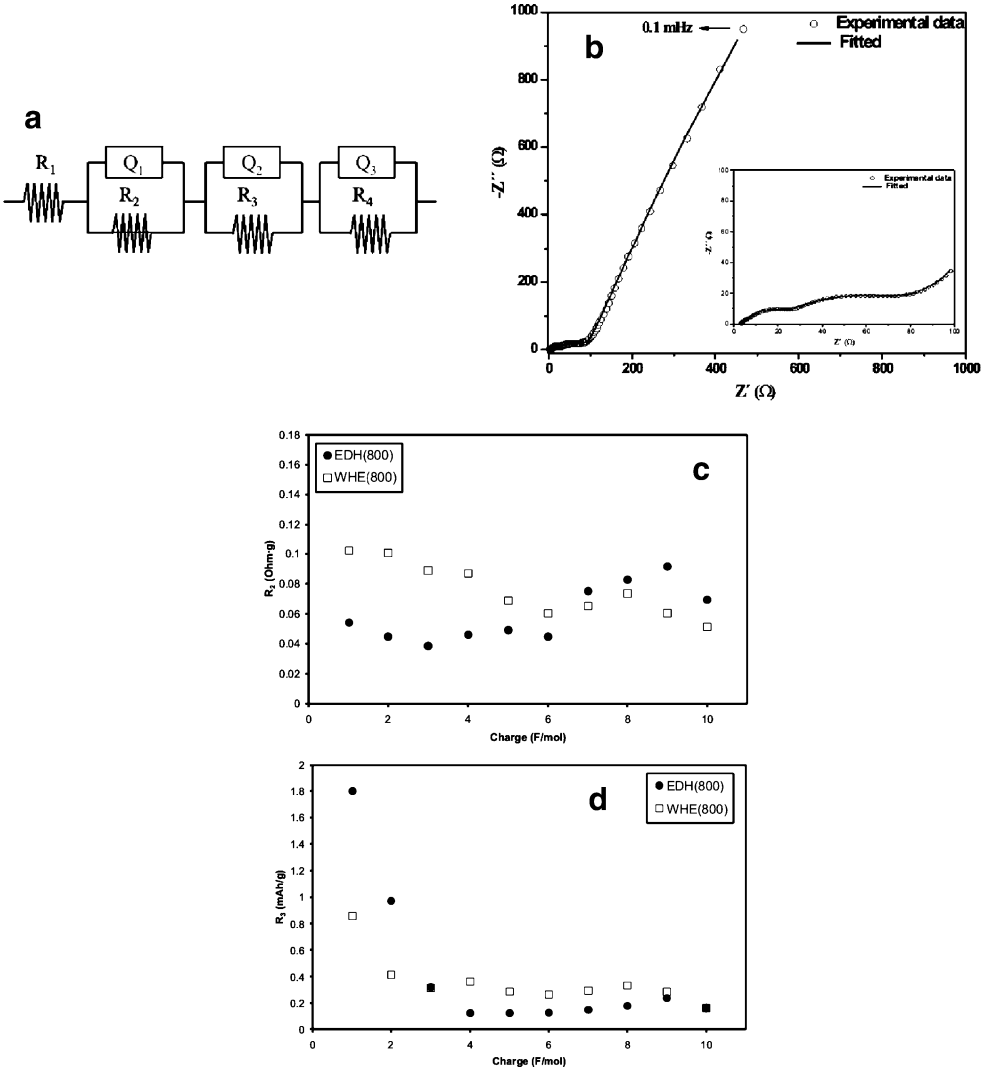

Fig. 8 **a** Analog equivalent circuit the experimental data; **b** Nyquist plot for fully discharged WHE(800) sample; **c** and **d** Variation of SEI and charge transfer resistance values during the first discharge

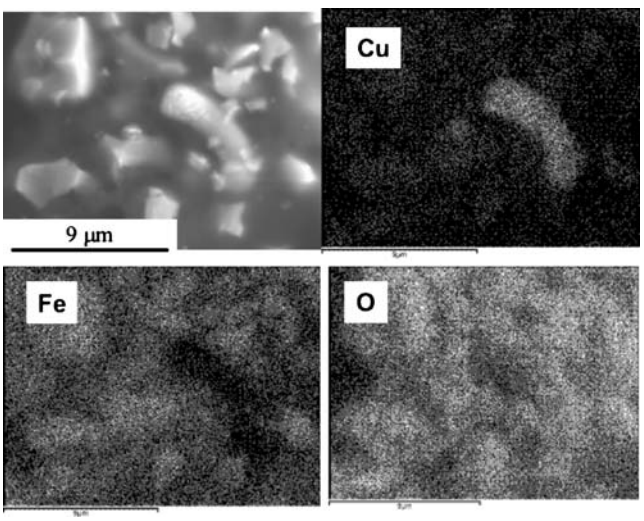

Fig. 9 SEM micrograph of WHE(1000) electrodes discharged at 0 V and EDS mappings for copper, iron and oxygen elements

aggregates mutually isolated by a surrounding gel-like substance ascribable to the referred polymeric layer formed at the end of the discharge. The nature of this layer has been described in the literature using several techniques, including electron microscopy [21, 28] and X-ray photoelectron spectroscopy [29]. The EDS mapping of the selected micrograph reveals the occurrence of copper-rich isolated particles. Some authors demonstrated the occurrence of reversible displacement reactions in copper containing compounds after lithium reaction. A high reversibility is related to the peculiar flexibility of the host structure [30]. This behavior would explain the presence of the copper-rich particles in the SEM image. The assignment of these copper particles to the presence of CuO impurities in the initial samples can be discarded from the observation of their XRD patterns. On the other hand, the lack of homogeneity in metal distribution at the end of the discharge may also negatively contribute to the electrochemical behavior on further cycling.

Conclusions

$CuFe_2O_4$ was prepared from two different citrate precursor obtained by either solvent evaporation or ethanol dehydration. Further annealing at temperatures from 600 to 1,000 °C evidenced significant changes in morphology hose influence in the electrochemical behavior, which was evaluated in lithium test cells.

Based on structural and morphological evidences, samples annealed at 800 °C were considered a priori more adequate for an optimal electrochemical performance. Thus, X-ray diffraction patterns revealed a low content of impurities, if any. In turn, SEM micrographs of EDH(800) evidenced the presence of submicron and/or nanosized particles. Their aggregation in secondary particles ensures a good connectivity, while forming a macroporous system that allows an extended electrode/electrolyte contact.

A noteworthy conclusion of this study is that the content of impurities of the original samples is less relevant for the electrochemical performance. This behavior is in contrast to what could be expected in other lithium reaction mechanisms, for instance, insertion. Thus, EDH samples retained high capacity values even if the impurities content was significant. In turn, the materials free from impurities obtained at 1,000 °C failed in providing high-performance electrodes due to the slow kinetic of the lithium reaction. EDH(800) materials performed capacity values after 50th cycles as high as 520 mAh/g. Their suitable morphologies and good kinetic response are the main factors favoring their better electrochemical performance.

Acknowledgement We acknowledge financial support from EC (contract SES6-CT2003-503532, ALISTORE), MEC (Contract MAT2005-00374), and Junta de Andalucía (FQM288 group). We also thank M.C. Mohedano for her technical support and the Central Services of Research of the University of Córdoba, and especially to F. Gracia and J. García, for the use of the electron microscopes and FTIR.

References

1. Thackeray MM, David WIF, Goodenough JB (1982) Mat Res Bull 17:785
2. Poizot P, Laruelle S, Grugeon S, Dupont L, Tarascon JM (200) Nature 407:496
3. Poizot P, Laruelle S, Grugeon S, Tarascon JM (2002) J. Electrochem Soc 149:A1212
4. Debart A, Dupont L, Patrice R, Tarascon JM (2006) Solid State Sci 8:640
5. Shao-Horn Y, Osmialowski S, Quinn CH (2002) J Electrochem Soc 149:A1547
6. Badway F, Pereira N, Cosandey F, Amatucci GG (2003) J Electrochem Soc 150:A1209
7. Pralong V, Souza DCS, Leung KT, Nazar LF (2002) Electrochem Commun 4:516
8. Aragón MJ, Pérez-Vicente C, Tirado JL (2007) Electrochem Commun DOI 10.1016/j.elecom.2007.03.031
9. Alcántara R, Jaraba M, Lavela P, Tirado JL (2002) Chem Mater 14:2847
10. Chadwick AV, Savin SLP, Fiddy S, Alcántara R, Fernández-Lisbona D, Lavela P, Ortiz GF, Tirado JL (2007) J Phys Chem C 111:4636
11. Alcántara R, Jaraba M, Lavela P, Tirado JL, Jumas JC, Olivier-Fourcade J (2003) Electrochem Commun 5:16
12. Alcántara R, Jaraba M, Lavela P, Tirado JL (2002) Solid State Chem 166:330
13. Larcher G, Sudant D, Leriche JB Chabre Y, Tarascon JM (2002) J Electrochem Soc 149:A234
14. Alcántara R, Lavela P, Tirado JL, Zhecheva E, Stoyanova R (1999) J Solid State Electrochem 3:121
15. Yue Z, Guo W, Zhou J, Zhilun G, Longtu L (2004) J Magn Magn Mater 270: 216
16. Zhecheva E, Stoyanova R, Gorova M, Alcántara R, Morales J, Tirado JL (1996) Chem. Mater 8:142
17. Dey S, Roy A, Das D, Ghose J (2004) J Mag Magn Mater 270:224
18. Hsuan-Fu Y, Shang-Wei Y (2005) J Alloys Compounds 394:286
19. Katkov AE, Lykasov AA (2003) Inorganic Materials 39:171
20. Mouallem-Bahout M, Bertrand S, Peña O (2005) J Solid State Chem 178:1080
21. Laruelle S, Grugeon S, Poizot P, Dollé M, Dupont L, Tarascon JM (2000) J Electrochem Soc 149:A627
22. Grugeon S, Laruelle S, Dupont L, Tarascon JM (2003), Solid State Sci. 5:895
23. Poizot P, Laruelle S, Grugeon S, Dupont L, Beaudoin B, Tarascon JM (2000) C R Chimie 3:681
24. Novak P (1985) Electrochim Acta 30:1687
25. Larcher D, Masquelier C, Bonnin D, Chabre Y, Masson V, Leriche JB, Tarascon JM (2003) J Electrochem Soc 150:A133
26. Concheso A, Santamaría R, Menendez R, Jiménez-Mateos JM, Alcántara R, Lavela P, Tirado JL (2004) Electrochim Acta 50:1225
27. McDonald JR (1987) Impedance Spectroscopy, Emphasizing Solid Materials and Systems. Wiley, USA
28. Débart A, Dupont L, Poizot P, Leriche JB, Tarascon JM (2001) J Electrochem Soc. 148:A1266
29. Dedryvere R, Laruelle S, Grugeon S, Poizot P, Gonbeau D, Tarascon JM (2004) Chem Mater 16:1056
30. Morcrette M, Rozier P, Dupont L, Mugnier E, Sannier L, Galy J, Tarascon JM (2003) Nature Materials 2:755